Journal of Ceramic Processing Research. Vol. 26, No. 4, pp. 573~585 (2025)
(Received 7 May 2025, Received in revised form 23 July 2025, Accepted 24 July 2025)
https://doi.org/10.36410/jcpr.2025.26.4.573

J O U R N A L O F
Ceramic Processing Research

Synergistic design and hydration mechanism of seawater-resistant low-heat cement using industrial byproducts

Peng-fei Zhao[a], Hai-tao Wang[a,*], Eng-dong Hua[b] and De-zhi Wang[b]
[a]*School of Traffic Engineering, Dalian Jiaotong University, Dalian 116000, China*
[b]*Dalian Product Quality Inspection and Research Institute Co. Ltd., Dalian 116000, China*

This study presents a seawater-resistant low-heat cement (SRLHC) synthesized from industrial byproducts, where blast furnace slag (73.3%) and fly ash (15%) were synergistically activated by a tailored silicate cement clinker-gypsum-sodium sulfate system (1%-4%-6.7%). Through D-optimal mixture design and seawater curing experiments, regression models correlating component ratios with compressive strength were established, yielding optimal 3-day and 28-day strengths of 27.3 MPa and 53.5 MPa, respectively. Microstructural characterization revealed a dual-phase hydration mechanism: 1) Initial hydration: Sodium sulfate reacted with clinker-derived $Ca(OH)_2$, generating an alkaline environment. This accelerated vitreous phase dissolution and led to the formation of ettringite (Aft) rods and calcium silicate hydrate (C-S-H) gels, which filled pores without expansive stress. 2) Long-term curing: Seawater-introduced $[SO_4]^{2-}$ reacted with residual Ca^{2+} to produce gypsum dihydrate, while continuous slag dissolution enhanced C-S-H gel formation, further densifying the matrix. Compared to conventional P·O 42.5 cement, SRLHC exhibited 40-47% higher strength and 105.4% seawater corrosion resistance, attributed to the synergistic interplay of Aft and C-S-H. This work provides a sustainable strategy for marine infrastructure by valorizing industrial solid wastes while addressing durability challenges in saline environments.

Keywords: Industrial solid waste, Optimal ratio, Heat of hydration, Seawater erosion resistance, Microstructure.

Introduction

With over 1.6 million km of global coastline and abundant marine resources, coastal nations are accelerating marine infrastructure construction under blue economy strategies. As the primary construction material, conventional marine Portland cement faces critical challenges: high clinker content in Portland cement, elevated hydration heat, insufficient early strength, slow or even retrogressive strength growth in seawater during later stages, relatively high production costs, significant energy consumption, and mediocre seawater corrosion resistance. Consequently, there is an urgent need to develop a marine cement with high early strength and superior seawater corrosion resistance.

The rapid expansion of global industrial capacity has generated 2.01 billion tons of solid by-products annually, with developing countries accounting for 63% of mismanaged wastes (World Bank, 2022). Solid waste stemming from industrial processes, which includes construction activities, not only exacerbates environmental crises but also leads to engineering cost overruns. Pollution caused by inadequate ISW management continues to intensify, disrupting ecological balance and posing severe threats to biodiversity and human health [1]. Particularly in tropical coastal regions, 28-34% of industrial residues (slags, silica fume, red mud) remain underutilized due to technical barriers in value-added applications. Our characterization of Indian thermal power plants reveals that 57% of Class F fly ash ($SiO_2+Al_2O_3>70\%$) and 41% of GGBS ($CaO/SiO_2=1.2$-1.6) meet ASTM C618/C989 specifications for cementitious applications. If highly reactive industrial solid waste is incorporated into mix designs for marine cement production, it could not only enhance the mechanical properties and seawater erosion resistance of the cement while reducing costs but also facilitate the resource utilization of solid waste [2-4].

Currently, numerous scholars have conducted extensive research on optimizing the composition of solid waste materials and activators that influence the strength performance of cement. In the selection of solid waste raw materials, Sun et al. [5] investigated the integration of ceramic waste, recycled glass cullet (RGC), and agricultural byproducts into bio-concrete for enhanced mechanical and durability performance. Experimental data showed progressive strength development: flexural strength increased from 2.5 MPa to 6.8 MPa and tensile strength from 2.0 MPa to 4.6 MPa across 7-, 28-, and 56-day curing. Concomitant improvements in chloride penetration resistance (reduced charge passage to 1000–2000 Coulombs) and sulfate durability (<0.5% mass

*Corresponding author:
Tel : +8615998581208
E-mail: 2849881024@qq.com

loss after exposure) were quantitatively demonstrated. Subashree et al. [6] demonstrated that 40% substitution of natural sand with waste ceramic tile (WCT) enhanced SCC compressive strength by 13.4% (49.25 MPa), reduced permeability to 32 mm (-29%), and lowered absorption to 2.25% (-36%). These gains are attributed to WCT-induced particle gradation optimization and pozzolanic densification, while maintaining workability compliant with EFNARC standards (slump flow: 674-733 mm; T500: 3.17-6.86 s). Anandaraja et al. [7] integrated coir fibers and finely ground ceramic waste powder (CWP) into concrete systems. CWP demonstrates distinct pozzolanic reactivity, while coir fibers provide natural crack-arresting capability. As a supplementary cementitious material, CWP confers dual sustainability advantages: reducing environmental impact and lowering production costs. Partial substitution of ordinary Portland cement (OPC) with CWP enables large-scale production of economical non-reinforced concrete. Yang et al. [8] engineered a novel fly ash-nanoclay composite through strategic integration of fly ash pellets within nanoclay ceramic insulation, yielding 22.5% energy savings in building envelopes via dual-action mechanisms: nanoceramic-mediated pore refinement (5-20 nm) and phase-change thermal modulation. Hale et al. [9] investigated whether the substitution limits of slag cement and fly ash are sufficient for concrete pavement and bridge structures. Their results indicate that the addition of slag cement generally has a positive effect on all cement types, while the incorporation of fly ash yields mixed outcomes. Kim et al. [10] Study comparing Ordinary Portland Cement (OPC), fly ash (FA) binary cement, fly ash/slag (GGBS) ternary cement, and low-heat cement (LHC) evaluated hydration heat reduction, performance, and durability. Results show the FA/GGBS ternary cement outperformed others, offering superior hydration heat mitigation and durability, making it optimal for mass concrete and durability-critical applications. Kavipriya et al. [11] incorporated slag and fly ash in concrete and demonstrated experimentally that Composite Concrete (CC) with 35% fly ash and 35% activated slag exhibited microscale bulge formations concurrent with Si-O-Al bond polymerization, enhancing compressive strength by 8.9% (to 43.87 MPa) and elastic modulus by 11.9% (to 29.35 GPa) relative to slag concrete (SC) controls. Gruyaert et al. [12] demonstrated that substituting blast furnace slag (BFS) for ordinary Portland cement (OPC) significantly alters the durability performance of concrete. Their findings revealed that BFS-based concrete exhibits markedly superior performance compared to OPC-based concrete when exposed to a lactic acid-acetic acid solution (pH ~2). Sabarinathan et al. [14] investigated the effect of partially replacing cement with Ground Granulated Blast Furnace Slag (GGBS) on the mechanical properties of concrete. Their results demonstrated that replacing 15 wt% of the cement with GGBS significantly enhanced mechanical performance compared to control concrete. They attributed this enhancement primarily to the angular morphology of the GGBS particles, which markedly improves interfacial adhesion within the cementitious matrix, thereby enhancing the overall concrete performance. Zhao et al. [13] demonstrated a synergistic 15-20% increase in the 70-day compressive strength of slag-limestone cement composites versus plain mortar. This resulted from $CaCO_3$ acting as nucleation sites densifying hydrates, while concurrent carbonate-slag reactions formed monocarboaluminate (Mc). MIP/NMR confirmed this synergy reduced pores >100 nm by 23-30%, refining pore structure and enhancing matrix densification. Han et al. [15] enhanced the strength and stability of slag cement by incorporating gypsum to promote ettringite formation. Liao et al. [16] developed a novel composite cementitious material by incorporating high proportions of phosphogypsum (40%-70% by mass), metallurgical waste slag (granulated blast furnace slag), and a calcium-based activator (hydrated lime). Experimental data revealed that as the phosphogypsum content increased gradiently, the hydration exothermic behavior of the system exhibited significant suppression. Notably, the group with 70% phosphogypsum content demonstrated continuous mechanical performance enhancement during a 90-day curing period, achieving a strength increase of 12.3%–27.8% compared to the 28-day baseline value. Jiang et al. [17] developed a marine-specific magnesium phosphate cement (MPC) system using a seawater-sea sand coupling preparation technique. Through systematic experiments, they comprehensively evaluated its hydration-hardening behavior and seawater erosion resistance. The results demonstrated that the marine MPC exhibited excellent resistance to seawater corrosion. However, its high production costs hinder its economic viability for large-scale marine engineering applications. Sulfoaluminate cement (CSA) is manufactured by crushing and grinding raw materials such as limestone, clay, iron-rich, and alumina-rich components, followed by calcination and the addition of appropriate amounts of gypsum. Primarily developed in China during the 1970s, CSA cement typically contains 50–80 wt% $C_4A_3\check{S}$ (calcium sulfoaluminate) and 10–30 wt% C_2S (belite). It is widely employed in engineering applications requiring rapid curing, early-stage strength development, or resistance to acidic/alkaline environments [18]. However, it exhibits higher production costs, significant performance degradation under high-temperature environments, and greater hydration heat compared to ordinary Portland cement (OPC). Saleh et al. [19] investigated the durability of ultra-high-performance seawater sea-sand concrete (UHP-SWSSC) with supplementary cementitious materials (SCMs) comprising ground blast furnace slag and silica fume. Mechanical and durability properties were evaluated through compressive testing of cubic specimens and durability experiments. Results indicate

that incorporating SCMs enhanced both mechanical performance and durability. At 50% cement replacement by SCMs, permeable void volume, water absorption, and non-steady-state chloride migration coefficient decreased by 53%, 75%, and 95%, respectively, compared to the control mix. Microstructural refinement from SCMs yielded a denser matrix, significantly impeding ionic penetration.

Shumuye et al. [20]'s review study demonstrates that incorporating industrial by-products such as ground granulated blast-furnace slag (GBFS) and fly ash (FA) as supplementary cementitious materials (SCMs) into environmentally sustainable Engineered Cementitious Composites (ECC) significantly enhances their durability in marine environments. The research indicates that SCMs improve resistance to sulfate attack, chloride ion penetration, and freeze-thaw cycles through microstructural refinement and reduced porosity connectivity, mechanisms attributed to their filler effect and pozzolanic reactions.

Ortega-López et al. [21] developed fiber-reinforced self-compacting concrete (FRSCC) using 100% electric arc furnace slag (EAFS) as both fine and coarse aggregates, and partial cement replacement with ground granulated blast-furnace slag (GGBFS). This approach yields an environmentally sustainable material with enhanced durability potential. Although GGBFS incorporation slightly elevates porosity (4.4% vs. 3.1% in OPC), it confers superior flexibility to the cementitious matrix. This intrinsic flexibility significantly improves resistance to sulfate attack and cyclic wet-dry conditions. Notably, the high-GGBFS concrete exhibited merely 7.42% strength loss after sulfate exposure, demonstrating exceptional sulfate resistance. In optimizing activators for Portland cement-slag composite systems, Sajedi et al. [22] demonstrated that sodium silicate ($Na_2SiO_3 \cdot nH_2O$) at 2–6% dosage increased 3-day flexural strength by 40–65% through enhanced pozzolanic activation, while NaOH underperformed (<15% strength gain) due to particle agglomeration. Tang et al. [23] demonstrated that citric (CA), tartaric (TA), oxalic (HAC), and EDTA acids significantly enhanced mechanical strength and water resistance in MOS cement. These additives promoted acicular 517-phase crystal growth while inhibiting the transformation of the $[Mg(H_2O)_xOH]^+$ hydration layer into brucite ($Mg(OH)_2$), thus optimizing cement performance. Sun et al. [19] reported sulfate activation generated corrosion-resistant crystalline phases. Tian et al. [25] investigated the impact of silicate modulus (M_s) in alkaline activators on fly ash-based geopolymer pastes (FGPs). SEM and XRD revealed that peak compressive strength (26.5-39.6 MPa at 28 days) occurred at M_s = 1.5 with 8.0-12.0 wt% Na2O (relative to fly ash), using a curing regime of 1 hour at 85°C followed by ambient conditions. Increased Na2O content accelerated fly ash dissolution and reaction kinetics, promoting denser sodium aluminosilicate hydrate (N-A-S-H) networks which enhanced matrix cohesion. Yu [26] and Li [27] optimized proportions of multi-component solid wastes using D-optimal mixture design, establishing quantitative frameworks for activator selection and waste material formulation.

In response to the global challenges of insufficient erosion resistance and poor environmental compatibility in marine engineering materials—particularly Portland cement, sulfoaluminate cement (CSA), and magnesium phosphate cement (MPC)—this study integrates the ecological characteristics of coastal zones and industrial solid waste management demands. We developed a novel seawater-resistant construction material by synergistically utilizing industrial solid wastes (slag, fly ash) with gypsum, Portland cement clinker, and anhydrous sodium sulfate.

A D-optimal mixture design was employed to investigate the 3-day and 28-day compressive strength of the cementitious composites under simulated seawater conditions, optimizing their formulations. Advanced characterization techniques, including X-ray diffraction (XRD) and scanning electron microscopy (SEM), were utilized to elucidate the seawater corrosion resistance mechanisms of the slag-rich low-heat cement (SRLHC).

The findings provide theoretical foundations for advancing the large-scale application of marine slag-based cement systems, addressing both durability limitations in harsh marine environments and sustainable utilization of industrial byproducts.

Materials and Methods

Materials

The experiment utilized Grade S95 ground granulated blast furnace slag powder (GGBS) supplied by Northeast Special Steel Group. Mineral composition analysis revealed a CaO/SiO_2 ratio of 1.17 (>1), classifying it as a typical alkaline slag system. Physical characterization indicated a bulk density of 2.87 g/cm^3, Blaine specific surface area of 419 m^2/kg, and an activity index (Ma value) of 79. Evaluated under the GB/T 203-2008 standard system, the slag powder demonstrated a quality coefficient (K) of 1.9, significantly exceeding the superior-grade threshold ($K \geq 1.8$), confirming its exceptional pozzolanic reactivity.

Table 1. Chemical composition of slag and coal ash (mass fraction).

	CaO	Al_2O_3	SiO_2	MgO	SO_3	Fe_2O_3	K_2O	Na_2O
GGBS	38.45	16.58	34.07	7.70	1.84	0.42	0.38	0.51
fly ash	5.10	35.33	46.57	0.83	1.75	4.15	0.35	0.61

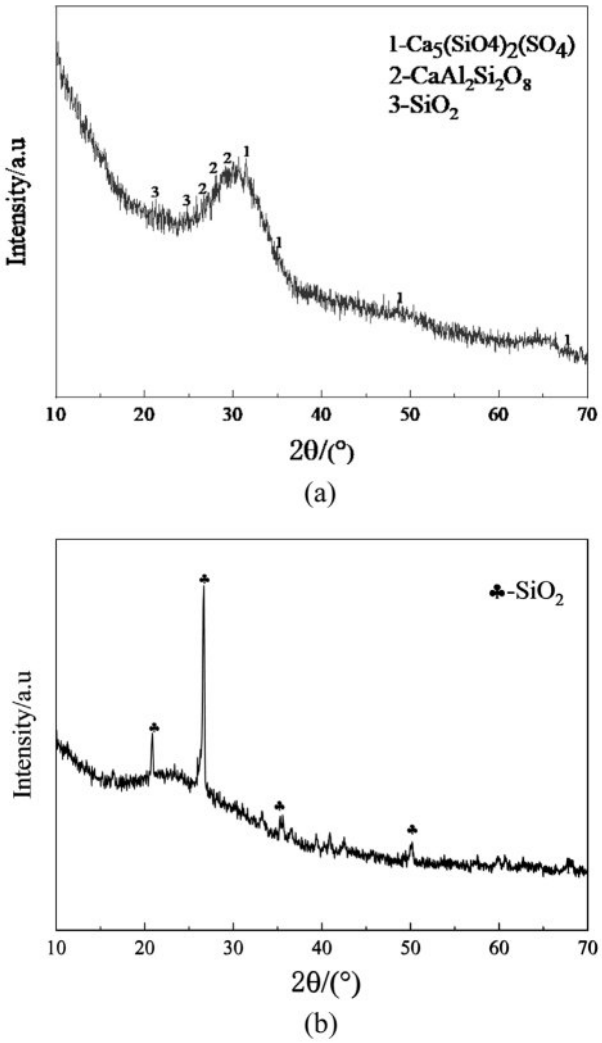

Fig. 1. XRD patterns of GGBS and fly ash.

ASTM C618-compliant Class F fly ash (median particle size 45 μm; sieve residue ≤ 1.5%), was employed. The principal chemical compositions of these raw materials are summarized in Table 1, with corresponding XRD patterns shown in Fig. 1. As illustrated in Figs. 1(a) and (b), the GGBS exhibited dominant crystalline phases of calcium silicate sulfate ($Ca_5(SiO_4)_2(SO_4)$), anorthite ($CaAl_2Si_2O_8$), and quartz (SiO_2), while the fly ash primarily consisted of crystalline SiO_2.

Activator

The selection of activators followed the criteria of high activation efficiency, wide availability, and environmental sustainability. Portland cement clinker, sodium sulfate, and gypsum were adopted as the primary activators in this study. The microstructural morphology observed via scanning electron microscopy (SEM) is illustrated in Fig. 2.

The Portland cement (P·O 42.5) was procured from Dalian Tianrui Cement Co., Ltd., China. Its specific surface area exceeded 350 m²/kg, with compressive

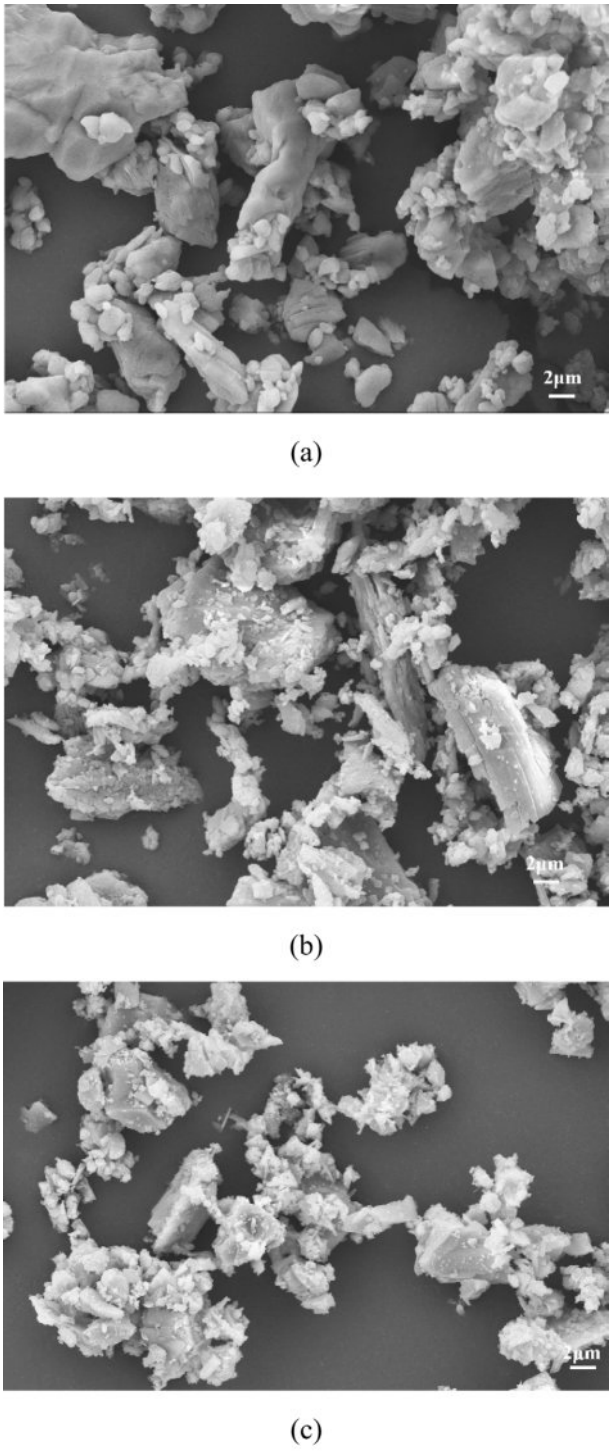

Fig. 2. Activator microstructure morphology.

strengths of ≥13 MPa at 3 days and ≥42.5 MPa at 28 days. The initial and final setting times were ≥45 min and 10 h, respectively. SEM analysis revealed that cement particles exhibited a polyhedral microcrystalline topological structure (Fig. 2a), facilitating the formation of high-specific-surface-area hydration products. These interlocked particles within bulk crystals enhanced intergranular bonding, thereby promoting dense packing of the cementitious matrix.

Gypsum, sourced from a local supplier in Dalian, displayed columnar and flaky morphologies with smooth surfaces (Fig. 2b). Under high-alkalinity conditions, gypsum effectively activated sulfate components, ensuring sustained release of SO_4^{2-} ions for ettringite (AFt) formation, which optimized the microstructure of the paste [28].

Anhydrous sodium sulfate (monoclinic crystal system, short columnar crystals) was supplied by a chemical manufacturer in Anhui Province. Its activation mechanism involved a reaction with portlandite [$Ca(OH)_2$] from cement hydration to generate NaOH. This alkaline environment accelerated the hydrolysis of glassy phases in slag and fly ash, yielding abundant C-S-H gels. Consequently, porosity was reduced, resulting in a more compact cement structure.

SRLHC strength proportioning test

Mixing and proportioning experiment

This experiment involves five variables: GGBS, fly ash, Portland cement clinker, gypsum, and anhydrous sodium sulfate. A D-optimal mixture design methodology was employed to investigate the relationship between the mass fractions of these components and the experimental performance indicators. This approach reduces experimental iterations, enhances prediction accuracy, and ensures sufficient data informativeness. Through limited experimental trials with varying component ratios, a regression model was successfully established to correlate the response variables (3-day and 7-day compressive strengths in seawater) with the proportions of constituents. The total mass percentage of all components was constrained to 100%.

Based on references [29-39], the compositional ranges were defined for seawater exposure optimization: (A) ground granulated blast furnace slag (GGBS, 0.60–0.80), (B) fly ash (FA, 0.10–0.25), (C) Portland cement clinker (0.01–0.03), (D) gypsum (0.04–0.07), and (E) sodium sulfate (Na_2O_4 0.04–0.075).

Mechanistic justifications are as follows:

GGBS (0.60–0.80) utilizes latent hydraulicity to form low-permeability C-A-S-H gel, achieving chloride diffusivity $<1.5 \times 10^{-12}$ m²/s and 28-day strength >55 MPa at >0.70 content [29-31]. FA (0.10–0.25) refines capillary porosity; at 0.10–0.15, it enhances workability (20% fluidity increase) and reduces chloride diffusivity by >40% versus plain cement [32]. Exceeding 0.25 FA, however, reduces 3-day strength by >19% relative to high-GGBS controls due to delayed pozzolanic reactions limiting early hydration [33, 34].

Clinker (0.01–0.03) provides critical alkalinity (pH >12) for GGBS activation while constraining syngenite ($K_2Ca(SO_4)_2 \cdot H_2O$) formation to prevent flash set above 0.03 [35]. Gypsum and Na_2SO_4 act synergistically: gypsum at 0.05–0.06 optimally supplies SO_4^{2-} for ettringite nucleation balancing strength and expansion, whereas Na_2SO_4 ≤0.075 accelerates C_3S hydration kinetics without inducing damaging crystallization pressure (>0.5 MPa) or microcracking [36-39].

Experimental factors implementing these ranges are detailed in Table 2.

Table 2. D-optimal mix design experimental factors and levels.

Factor	mass fraction (%)	
	min	max
GGBS mass fraction%	60	80
Fly ash mass fraction%	10	25
Cement mass fraction%	1	5
Gypsum mass fraction%	4	7
Sodium sulfate mass fraction%	4	7.5

Test results and analysis

Following the D-optimal mixture design protocol, raw materials were proportioned by mass and homogenized in a cement mortar mixer with controlled water addition to obtain a homogeneous paste. The blended slurry was subsequently poured into triple molds (7.07 cm × 7.07 cm × 7.07 cm) and consolidated through vibration. The cast specimens, along with molds, were cured in a standard climate chamber at 20 ± 1 °C with 90% relative humidity for 24 h.

After demolding, specimens were immediately immersed in natural seawater collected from Dalian, China, for 3-day and 28-day curing periods. Mechanical testing was performed according to Chinese National Standard GB/T 17671-2021 [40], wherein uniaxial compressive strength was measured using a servo-controlled testing machine at a loading rate of 2.4 kN/s.

The compressive strength values at specified curing ages are plotted in Fig. 3.

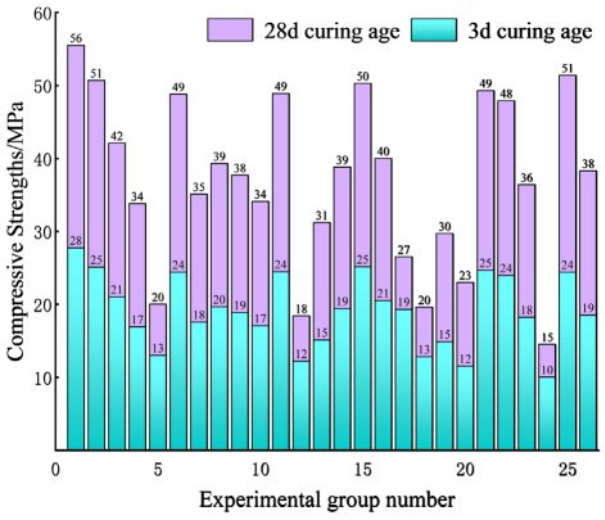

Fig. 3. Compressive Strengths results of mixture ratio groups 1~26.

Analysis of variance

To evaluate seawater corrosion resistance of the developed low-heat cement, 25 mixture formulations were designed using D-optimal criteria, with an additional control group (P·O 42.5 ordinary Portland cement) establishing 26 experimental systems. For each mixture, compressive strength was determined from the average of three independent tests at each curing age. To assess the reliability of these measurements, the relative standard deviations (RSD) for the compressive strengths of SRLHC at 3 days (Y3d) and 28 days (Y28d) were calculated. Importantly, all RSD values were below 3%, demonstrating good experimental repeatability. Compressive strength data at 3-day (Y3d) and 28-day (Y28d) curing periods were obtained through standardized testing (Fig. 3). The Y3d values ranged from 10 to 27.75 MPa, while Y28d exhibited 14.5–55.5 MPa, corresponding to strength growth rates of 37.31%–110.66%. Notably, the SRLH cement demonstrated superior strength development compared to the P·O 42.5 control (51.7% growth rate).

The reliability of mathematical models was verified through analysis of variance (ANOVA). Table 3 presents ANOVA metric for cubic regression models of Y3d and Y28d. At a significance level α=0.05, model term significance was determined by F-value and p-value thresholds: terms with $p<0.05$ and $F>F_{critical}$ were considered statistically significant, while those with $p>0.1$ were eliminated [27]. Through stepwise elimination of insignificant terms, optimized third-order regression equations were derived as:

$$Y3d = 24.29A + 14.37B + 224.76C - 189.07D - 110.58E - 355.38AC + 259.76AD + 177.89AE - 260.90BC + 245.74BD + 238.12BE$$

$$Y28d = 45.42A - 10.31B + 1288.02C - 838.38D - 768.16E + 66.12AB - 1698.75AC + 1041.34AD + 961.84AE - 1447.04BC + 1284.67BD + 1299.49BE - 1186.22CD - 363.97CE + 958.74DE$$

The regression models exhibited strong explanatory power, with R-squared (R^2) values of 0.88 for Y3d and 0.95 for Y28d. Both coefficients exceeding the 0.8 threshold demonstrate the model's effectiveness in characterizing the intrinsic relationships between system responses (compressive strength) and compositional variables, suggesting adequate predictive capability for multi-component cementitious systems under seawater exposure.

Interactions

Two-factor interaction analysis

Fig. 4 shows the compressive strength evolution curves of seawater-cured low-heat Portland cement under binary factor interactions. The slag-Portland composite system (Figs. 4a, h) demonstrates similar response patterns in dual-age strength development: With increasing slag proportion and decreasing Portland component, the

Table 3. Analysis of variance for Y3d and Y28d.

Source	Y3d		Y28d		Remark
	F ratio	P ratio	F ratio	P ratio	Significant
Model values	10.69	< 0.0001	16.81	< 0.0001	—
Linear mixture	19.81	< 0.0001	37.01	< 0.0001	—
AB	—	—	8.51	0.0154	—
AC	18.56	0.0007	29.44	0.0003	—
AD	6.11	0.0269	6.08	0.0334	—
AE	5.29	0.0374	10.16	0.0097	—
BC	11.78	0.004	22.42	0.0008	—
BD	4.77	0.0464	9.21	0.0126	—
BE	9.61	0.0078	18.28	0.0016	—
CD	—	—	3.8	0.0798	—
CE	—	—	5.84	0.0624	—
DE	—	—	4.36	0.0633	—
Residual	—	—	—	—	—
Lack of fit	5.68	0.0544	5.4	0.0624	Not significant
$_{Y3d}R^2$=0.88		$_{Y3d}R_{Adj}{}^2$=0.87		$_{Y3d}R_{Pred}{}^2$=0.83	
$_{Y28d}$R2=0.96		$_{Y28d}$RAdj2=0.95		$_{Y28d}$RAdj2=0.94	

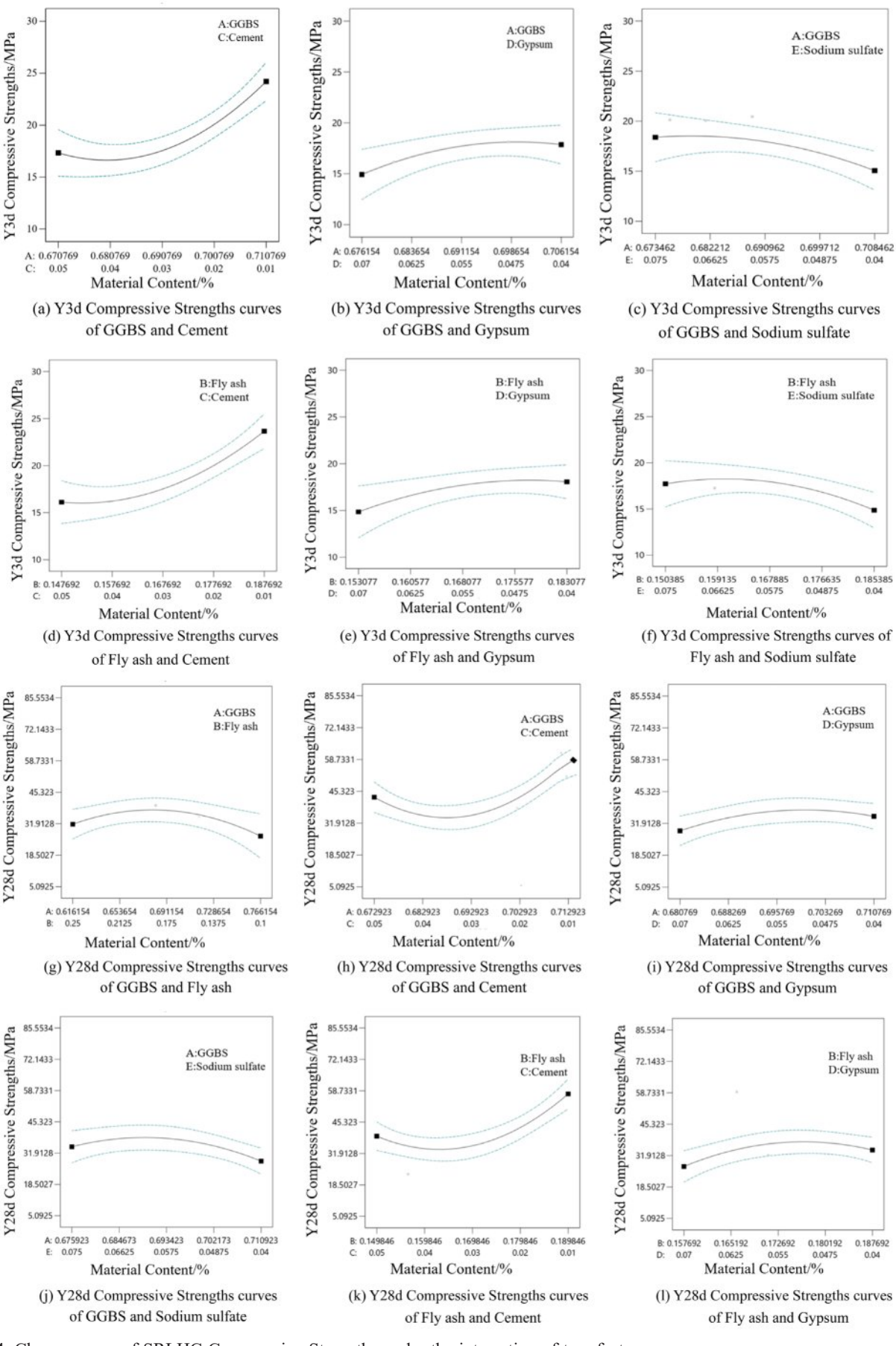

Fig. 4. Change curve of SRLHC Compressive Strengths under the interaction of two factors.

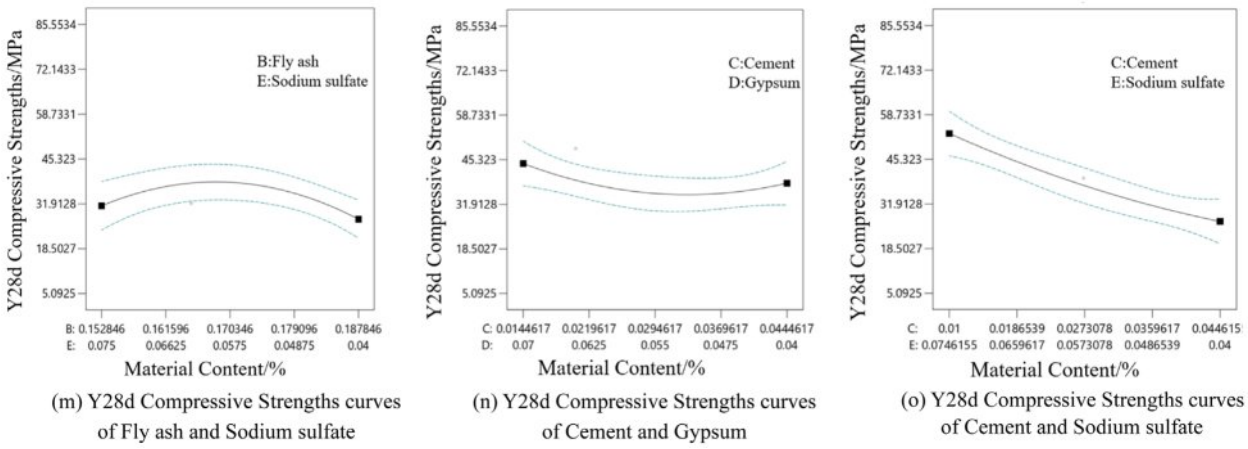

(m) Y28d Compressive Strengths curves of Fly ash and Sodium sulfate

(n) Y28d Compressive Strengths curves of Cement and Gypsum

(o) Y28d Compressive Strengths curves of Cement and Sodium sulfate

Fig. 4. Continued.

compressive strength curve exhibits typical parabolic characteristics, where the 28-day strength extremum confirms the existence of an optimal mix ratio threshold in this system.

The fly ash-Portland system (Figs. 4d, k) displays differential regulatory effects, showing significant sensitivity to fly ash content variations in early-stage strength development. Its strength evolution presents a two-phase pattern of gradual decline followed by steep ascent. The combined incorporation of slag and gypsum produces differentiated effects on early (3-day) and long-term (28-day) compressive strengths.

Strength evolution patterns revealed in Figs. 4(c) and (g) indicate a significant negative correlation between specimen strength and slag content at 3-day curing. Long-term strength tests (28-day) demonstrate nonlinear variation rules in the synergistic interaction between slag and sodium sulfate. Experimental observations confirm that when slag content progressively increases while sodium sulfate content correspondingly decreases, the compressive strength shows characteristic trend of initial increase followed by decrease, verifying the existence of a specific optimal proportion range in this binary cementitious system.

As shown in Figs. 4(b) and (i), the combined effect of decreasing slag content and increasing gypsum dosage exerts minimal influence on compressive strength, with Y28d strength showing only minor fluctuations (3.2-6.4% variation). This indicates weak synergy between these components, making them unsuitable for standalone combination.

Figs. 4(e, l, f, m) reveal that the incorporation of fly ash with gypsum, and fly ash with sodium sulfate, exhibit similar impacts on compressive strength at Y3d and Y28d curing ages respectively. When fly ash dosage increases while gypsum decreases, both 3-day and 28-day compressive strengths show initial enhancement followed by reduction. Similarly, increasing fly ash with decreasing sodium sulfate produces analogous strength variation patterns. These phenomena confirm the existence of optimal mixing ratios for both material combinations (fly ash+gypsum and fly ash+sodium sulfate) at their respective curing ages.

Five-factor interaction analysis

Fig. 5 illustrates the compressive strength evolution curves of seawater-resistant low-heat cement under the interactive effects of five factors during seawater curing. At the 3-day curing age (Fig. 5a), the influence of GGBS on compressive strength (Y3d) is most significant, followed by sodium sulfate. The Y3d strength initially decreases and then increases with rising GGBS content, indicating a maximum strength within the GGBS dosage range of 70%~80%. Conversely, fly ash exhibits an opposing trend: Y3d reaches a minimum within 10%~17% fly ash content and a maximum at 17%~25%. Sodium sulfate demonstrates a parabolic relationship, with Y3d peaking at 4%~7.5% dosage. Portland cement clinker shows a sharp initial decline followed by gradual recovery in Y3d, yielding a maximum at 1%~2% and a minimum at 2%~3%. Dihydrate gypsum inversely affects Y3d, achieving maximum strength enhancement at 4%~5%.

For the 28-day curing age (Fig. 5b), analogous optimization ranges emerge: maximum compressive strength (Y28d) occurs at GGBS dosages of 69%~80%, sodium sulfate 5%~7.5%, Portland cement clinker 1%~2%, dihydrate gypsum 4%~5%, and fly ash 17%~25%. These results systematically quantify the synergistic effects of multi-component interactions on long-term mechanical performance in marine environments.

Optimal ratios and validation

Through ANOVA and multi-factor, multi-response joint optimization of SRLHC, the results were refined to meet all numerical requirements for the response variables, thereby obtaining the optimal formulation for comprehensive SRLHC performance. Multi-factor collaborative optimization was performed using Design

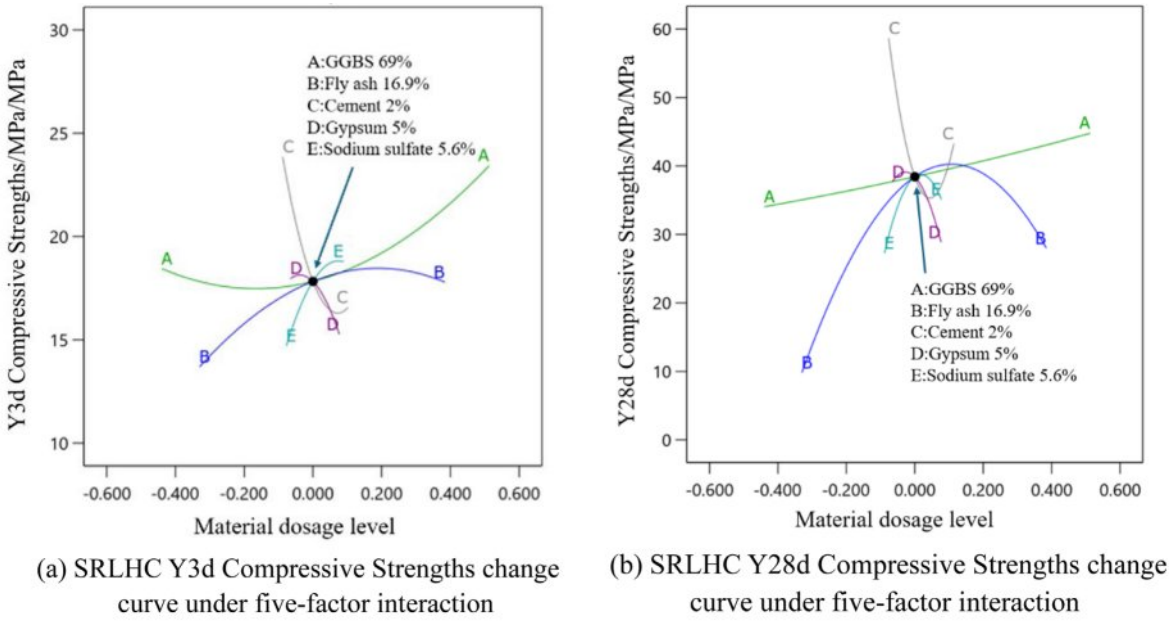

(a) SRLHC Y3d Compressive Strengths change curve under five-factor interaction

(b) SRLHC Y28d Compressive Strengths change curve under five-factor interaction

Fig. 5. Effect of GGBS, fly ash, Cement, gypsum and sodium sulfate on the strength of SRLHC.

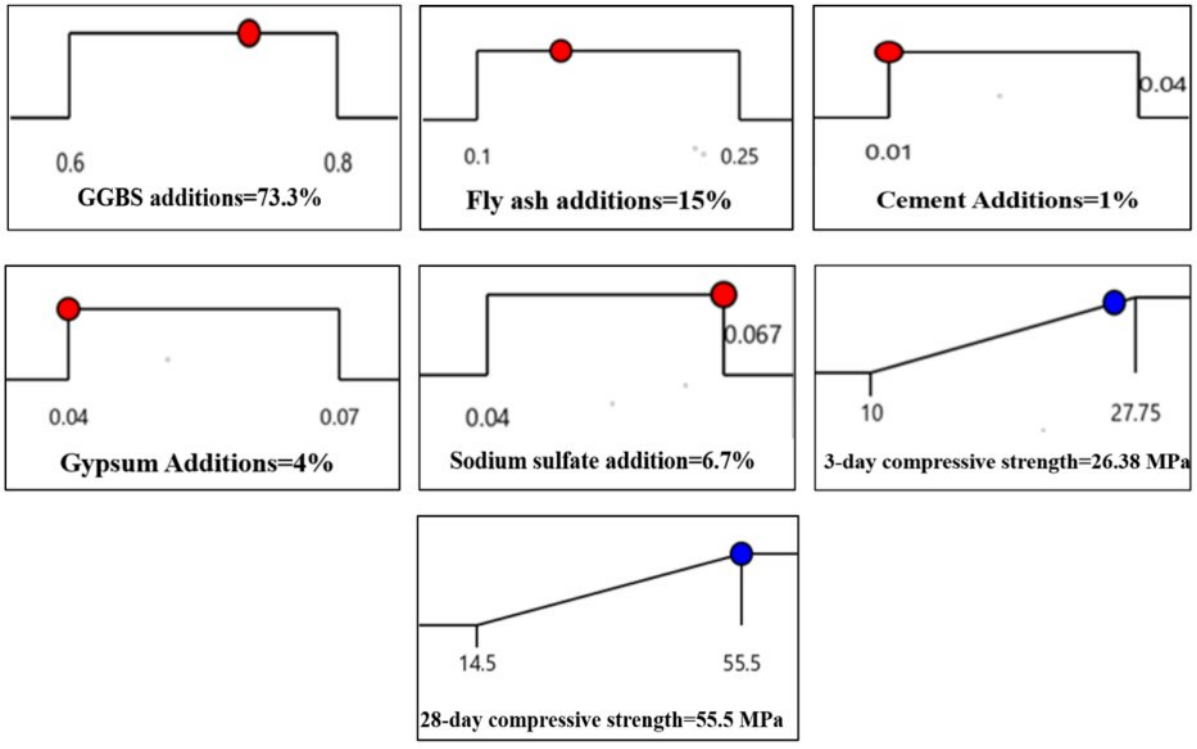

Fig. 6. D-Optimal methodology to optimize SRLHC proportioning design.

Expert software. Given the primary objective of studying SRLHC's seawater erosion resistance, the response value ranges were maximized to ensure optimal performance across all metrics. The optimization criteria, as illustrated in Fig. 6, yielded the optimal formulation: 73.3% GGBS, 15% fly ash, 1% Portland cement clinker, 4% gypsum, and 6.7% sodium sulfate. Experimental validation using this formulation was conducted based on the predicted values of the optimized scheme, with the results summarized in Table 4.

Experimental validation using this mix ratio was performed against predicted values, with results summarized in Table 4. The table clearly demonstrates that the measured 3-day (Y3d) and 28-day (Y28d)

Table 4. Comparison of optimization design and actual results.

Peer group		Optimal proportions group			Cement group
Y3d Compressive Strengths/MPa	predictions	26.38			
	Actual	27.3			18.5
Y28d Compressive Strengths/MPa	predictions	55.5			
	Actual	53.5			38.3
Actual Errors	Y3d	0.92	Y7d	-2	
Percentage of error		3.5%		3.6%	

compressive strengths exhibit errors within 5% compared to predictions, confirming the high accuracy of the response surface methodology (RSM) in optimizing SRLHC formulations and validating the model's precision.

Comparative analysis with a cement control group reveals that the Y3d strength of SRLHC is 1.47 times that of the control, while Y28d strength is 1.4 times higher. This shows that SRLHC exhibits superior seawater corrosion resistance.

Durability Assessment

To evaluate the durability of specimens with the optimized mix ratio, constituent materials were proportioned, mixed with water in a cement mortar mixer, and homogenized. The paste was cast into 7.07 cm^3 triple molds. Specimens underwent initial curing under controlled conditions (20 °C, 90% RH) within molds. After 24 h demolding, specimens were immersed separately in Dalian seawater or deionized water for 28 days. Uniaxial compressive strength of these water-cured specimens was then determined per Chinese National Standard GB/T 17671-2021 [40] (equivalent to ISO 679:2009).

As shown in Table 5, optimized-mix specimens exhibited compressive strengths >51 MPa after 28 days in both immersion media. Evaluation of seawater erosion resistance followed Chinese National Standard GB/T 38140-2019 [41]. The compressive strength retention rate of the seawater-resistant low-heat cement (SRLHC) was 105.4%, further confirming its superior performance in resisting seawater degradation.

Table 5. Optimal mix ratio of cement test blocks under different curing conditions: 28-day compressive strength.

Conservation condition	Deionized water maintenance	Marine water conservation
Y28d Compressive Strengths/MPa	51.9	53.4
	51.4	53.1
	52.3	53.0
	55.4	52.5
	55.4	51.7
	57.2	54.0
average value	52.5	54.4

Microscopic experimental studies

Physical phase analysis

The optimal mix ratio obtained via the D-Optimal method was used to prepare specimens, which were subjected to XRD testing after 3-day and 28-day seawater curing alongside a P·O 42.5 cement control group. As shown in Fig. 7, prominent diffraction peaks of ettringite and calcium silicate hydrate (C-S-H) were observed. Comparative analysis with P·O 42.5 cement's XRD patterns reveals that only C-S-H diffraction peaks were detected during the initial hydration stage of P·O 42.5 cement, with no ettringite peaks observed. This indicates minimal or no ettringite formation in early-stage P·O 42.5 cement hydration, resulting in insufficient framework formation and low early strength. Residual C3S peaks observed in later hydration stages demonstrate incomplete hydration of P·O 42.5 cement. The appearance of Aft diffraction peaks near 30° suggests late-stage ettringite formation in P·O 42.5 cement, potentially increasing cracking risks.

In contrast, SRLHC specimens showed no detectable Na_2SO_4 or $Ca(OH)_2$ diffraction peaks but exhibited abundant ettringite diffraction peaks (15°-43°). This confirms that sodium sulfate exerts catalytic effects during early hydration in the SRLHC system. During

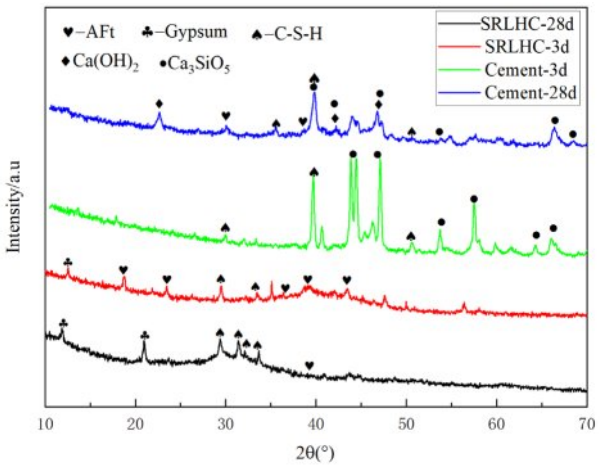

Fig. 7. XRD spectra of cement and SRLHC at curing ages of 3 and 28 d.

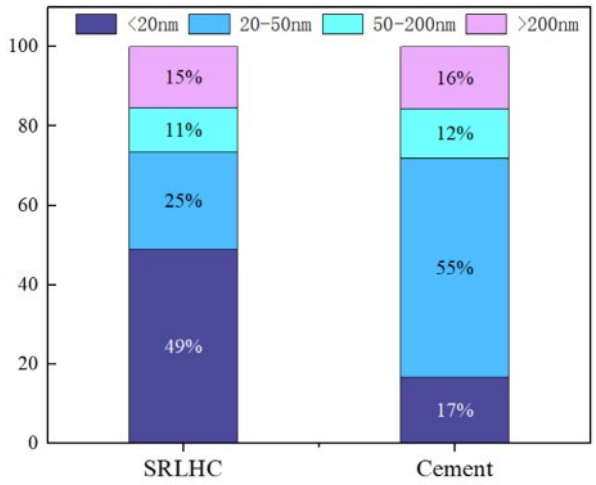

Fig. 8. Aperture gradation of SRLHC and cement at curing age of 28d.

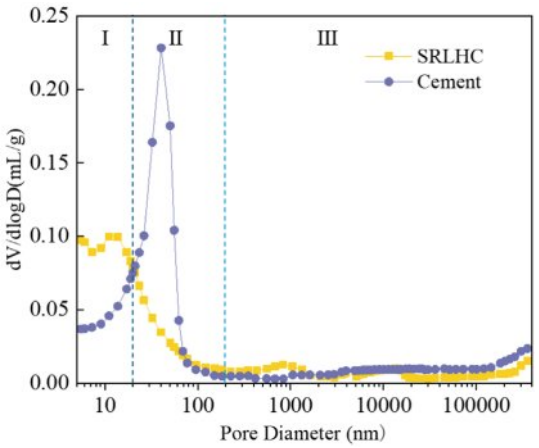

Fig. 9. Pore size distributions of SRLHC and cement at curing age of 28d.

hydration, calcium hydroxide coordinates with sulfate ions to form gypsum dihydrate crystals. Upon reaching critical concentration, these crystals react with AFm (monosulfur type hydrated calcium sulfoaluminate) phases to form ettringite structures. This mechanism ensures exclusive ettringite formation rather than AFm during initial hydration. The co-precipitation of gypsum dihydrate and ettringite effectively fills internal pores, enhancing structural density and consequently improving compressive strength during early seawater exposure [24].

Notably, SRLHC specimens exhibited significantly intensified C-S-H diffraction peaks near 32° during later hydration stages compared to initial phases. This demonstrates continuous dissolution of Ca^{2+}, $[Si(OH)3O]^-$ and $[Al(OH)_4]^-$ from GGBS and fly ash, driving sustained pozzolanic reactions that generate additional C-S-H to refine pore structures. Only gypsum dihydrate peaks were detected near 12°, with no excessive ettringite formation observed. This indicates that seawater sulfate ions primarily react with calcium hydroxide to form limited gypsum dihydrate during later SRLHC hydration, without inducing destructive ettringite crystallization. The absence of significant microstructural deterioration explains SRLHC's superior seawater erosion resistance [42].

Microstructural analysis

The pore structure characteristics of cementitious materials are intrinsically linked to their mechanical performance [43]. Mercury intrusion porosimetry (MIP) tests were performed on 28-day seawater-cured specimens. Pores were classified per Wu Zhongwei's criteria: harmless (<20 nm), slightly harmful (20-50 nm), harmful (50-200 nm), and extremely harmful (>200 nm) [44]. Fig. 8 shows the quantified pore size distributions [6]. For clarity, pores of 20-200 nm were grouped as "harmful" in the continuous distribution curves (Fig. 9).

Data reveal that SRLHC exhibits 49% harmless pores (vs. 17% in control) and 36% harmful pores (vs. 67% in control), indicating a 32% increase in harmless pores and 31% reduction in harmful pores. Critically, the most probable pore size of SRLHC (the peak in Fig. 9) is 13.77 nm, which is significantly lower than that of the control sample (40 nm) and falls below 20 nm, indicating that SRLHC forms a finer pore structure. According to the research of Wang Lei [45] gel pores smaller than 20 nm are mainly generated by calcium silicate hydrate (C-S-H). The results of this study (i.e., the most probable pore size of SRLHC is 13.77 nm, which is within this range) strongly suggest that SRLHC contains a higher content of C-S-H in its hydration products and exhibits more sufficient hydration development. The SEM observation results further confirm this point.

Fig. 10 presents SEM images of cement and SRLHC at different curing ages in seawater. Comparative analysis reveals distinct microstructural differences. For ordinary P·O 42.5 cement at early hydration stages (3d), abundant pores dominate the microstructure, accompanied by minimal ettringite formation and residual tricalcium silicate (C_3S) particles. In contrast, the 3d SEM image of SRLHC exhibits individually distributed, slender rod-shaped ettringite crystals with free growth at both ends, forming an effective skeletal framework. Concurrently, calcium silicate hydrate (C-S-H) and gypsum fill the interstitial pores, resulting in a significantly denser structure.

At later hydration stages, SEM images of ordinary P·O 42.5 cement display extensive cracks and pores alongside ettringite formation. This observation aligns with XRD analysis (Fig. 7), confirming that late-stage ettringite generation in P·O 42.5 cement exacerbates cracking risks. Conversely, the 28d SEM image of SRLHC shows no detectable ettringite formation. Its microstructure achieves remarkable densification, with pores nearly fully occupied by C-S-H and gypsum. This pore-filling mechanism enhances structural integrity,

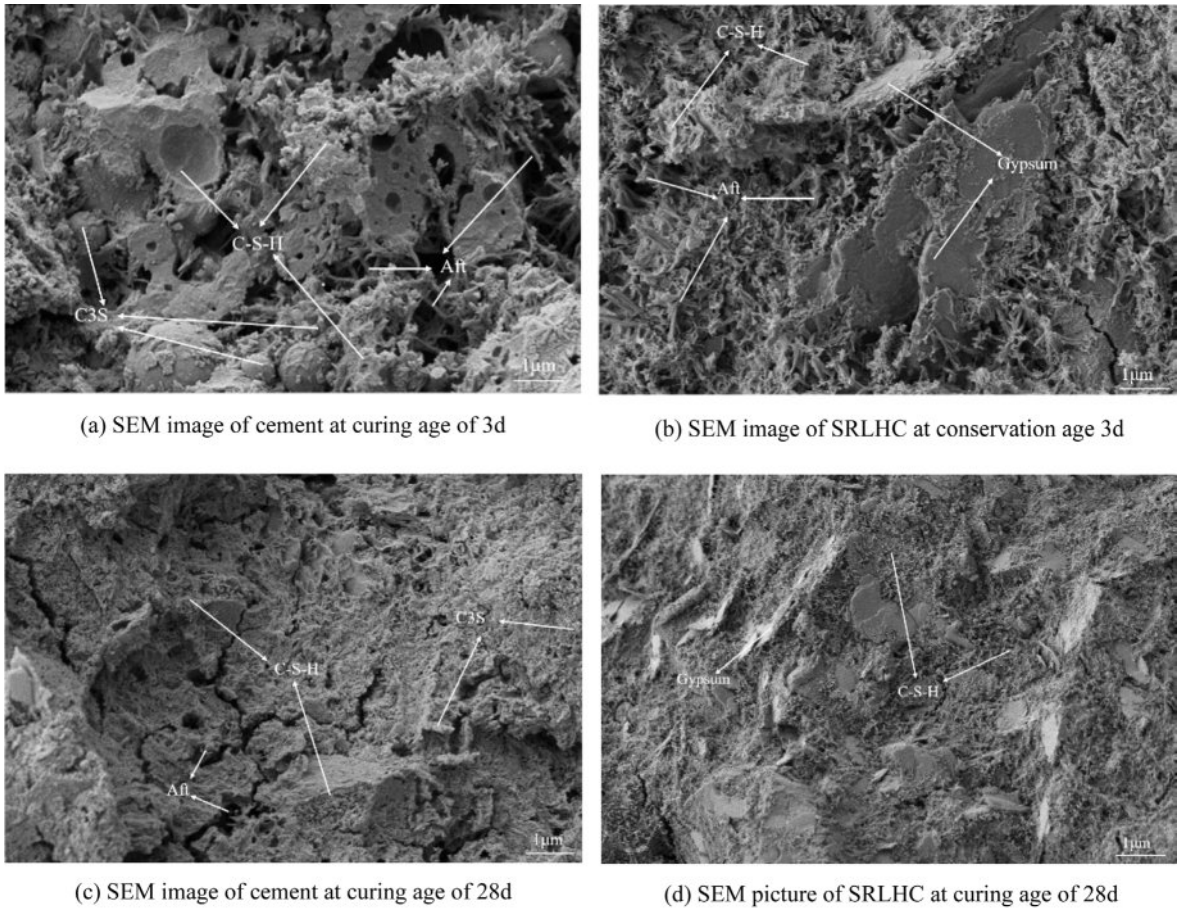

Fig. 10. SEM pictures of cement and SRLHC at different maintenance ages.

directly contributing to SRLHC's superior resistance to seawater erosion.

Conclusion

Through the D-optimal mixture design experimental protocol, a multi-factor and multi-response joint optimization was conducted, establishing quadratic polynomial models for SRLHC's 3-day and 28-day compressive strengths under seawater curing. Both models exhibited regression coefficients R^2>0.8, indicating high model accuracy and excellent fitting performance.

With SRLHC's compressive strength as the optimization objective and the contents of GGBS, fly ash, Portland cement clinker, gypsum, and anhydrous sodium sulfate as variables, the numerical optimization function yielded an optimal formulation: 73.3% GGBS, 15% fly ash, 1% Portland cement clinker, 4% gypsum, and 6.7% sodium sulfate. Under this formulation, the 3-day and 28-day compressive strengths of SRLHC in seawater reached 26.38 MPa (+47% vs control) and 55.5 MPa (+40% enhancement), respectively. Multiple validation tests confirmed deviations between measured and predicted values within 5%, further demonstrating the model's reliability and predictive precision.

XRD and SEM analyses revealed that SRLHC exhibits superior seawater erosion resistance compared to ordinary 425 cement, primarily attributed to its hydration products—ettringite (Aft) and C-S-H gel. During early hydration, sodium sulfate reacts with hydration products of the cement clinker to create an alkaline environment.

$$Na_2SO_4 + Ca(OH)_2 + 2H_2O \rightarrow 2NaOH + CaSO_4 \cdot 2H_2O\downarrow \quad (1)$$

This dual mechanism accelerates hydrolysis of the raw material's vitreous phases and facilitates the reaction between calcium aluminate hydrate, calcium sulfate, and OH^-, yielding optimal quantities of calcium sulfoaluminate hydrate (ettringite).

$$SiO_2 + H_2O + OH^- \rightarrow [Si(OH)_3O]^- \quad (2)$$

$$Al_2O_3 + 3H_2O + 2OH^- \rightarrow 2[Al(OH)_4]^- \quad (3)$$

$$[Si(OH)_3O]^- + Ca^{2+} + OH^- \rightarrow CaO \cdot SiO_2 \cdot H_2O\ (C\text{-}S\text{-}H) + H_2O \quad (4)$$

$$2[Al(OH)_4]^- + 6Ca^{2+} + 3SO_4^{2-} + 4OH^- + 26H_2O \rightarrow Ca_6Al_2(SO_4)_3(OH)_{12} \cdot 26H_2O \quad (5)$$

The ettringite formed in this system adopts slender, individually distributed rod-shaped crystals with

unrestricted growth at both ends, significantly reducing crystalline growth stress and minimizing expansive effects within the cement matrix. Synergizing with C-S-H gel, this microstructure achieves pore densification, thereby enhancing the 3-day compressive strength in seawater.

In later hydration stages, seawater-derived $[SO_4]^{2-}$ reacts with calcium hydroxide in SRLHC to form limited gypsum dihydrate, without triggering ettringite formation. This process avoids significant microstructural damage. Concurrently, continuous dissolution of Ca^{2+}, $[Si(OH)_3O]^-$, and $[Al(OH)_4]^-$ from blast furnace slag and fly ash drives sustained pozzolanic reactions, generating additional C-S-H to further refine pore structures. The resultant densification leads to a marked improvement in the 28-day compressive strength under seawater exposure.

Acknowledgments

This work was supported by the Liaoning Provincial Administration for Market Regulation Science and Technology Program (Grant number. 2023ZC024). Support from the Dalian Product Quality Inspection and Testing Institute and the School of Traffic Engineering, Dalian Jiaotong University is also gratefully acknowledged.

References

1. S. Janania, G.S. Rampradheep, P. Kulanthaivel, and P.C. Murugan, J. Ceram. Process. Res. 23[6] (2022) 884-891.
2. K. Yuvaraj and S. Ramesh, Cem. Wapno. Beton. 3 (2021) 253-262.
3. D. Velumani, P. Mageshkumar, and K. Yuvaraj, Pol. J. Environ. Stud. 33[1] (2024).
4. A.A.M. Fazli, S.K. Zakariaa, N.I.N.A. Rahmana, S.Z. Salleha, A.H. Yusoffa, N.A. Sallehb, M.A.A. Taibc, F. Budimand, A. Alia, and P.T. Teo, J. Ceram. Process. Res. 21[6] (2020) 667-682.
5. F. Sun and J. Lin, J. Ceram. Process. Res. 26[2] (2025) 295-298.
6. P. Subashree, V. Sampathkumar, S. Gowtham, A.A. AlObaid, and I. Warad, J. Ceram. Process. Res. 25[2] (2024) 220-227.
7. S. Anandaraja, A.R. Krishnaraja, P. Kulanthaivel, and P.C. Murugan, J. Ceram. Process. Res. 25[1] (2024) 41-47.
8. W. Yang and J. Chen, J. Ceram. Process. Res. 25[5] (2024) 727-736.
9. W.M. Hale, S.F. Freyne, and T.D. Bush, Constr. Build. Mater. 22[9] (2008) 1990-2000.
10. C.H. Kim and N.W. Kim, J. Korean Inst. Resour. Recycl., 23[3] (2014) 13-20.
11. S. Kavipriya, K. Pradeep, and S. Southamirajan, J. Ceram. Process. Res. 26[1] (2025) 1-8.
12. E. Gruyaert, P.V.D. Heede, M. Maes, and N. De Belie, Cem. Concr. Res. 42[1] (2012) 173-185.
13. K. Sabarinathan and G. Arunkumar, J. Ceram. Process. Res. 24[2] (2023) 390-396.
14. Y. Zhao, X. Yue, Y. Tang, X. An, and X. Shang, J. Ceram. Process. Res. 25[5] (2024) 862-870.
15. D. Han, G.C. Lee, and G.Y. Lee, J. Ceram. Process. Res., 17[2] (2016) 129-137.
16. Y. Liao, K. Wang, and H. Li, Bull. Chin. Ceram. Soc. 42[12] (2023) 4408-4415.
17. J. Jiang, M. Xue, and H. Wang, J. Funct. Mater. 43[7] (2012) 828-834. (in Chinese)
18. M.A.G. Aranda and A.G. De la Torre, Eco-Efficient Concrete (2013) 488-522.
19. S. Saleh, A.H. Mahmood, X.-L. Zhao, and E. Hamed, Mater. Today: Proc. (2023).
20. E.D. Shumuye, W. Li, G. Fang, Z. Wang, J. Liu, and K. Zerfu, Case Stud. Constr. Mater. 19 (2023) e02324.
21. V. Ortega-López, F. Faleschini, C. Pellegrino, V. Revilla-Cuesta, and J.M. Manso, Constr. Build. Mater. 320 (2022) 126280.
22. F. Sajedi and H.A. Razak, Constr. Build. Mater. 24[10] (2010) 1944-1951.
23. Y. Tang, X. Yue, Y. Zhao, X. An, X. Shang, and C. Liu, J. Ceram. Process. Res. 26[2] (2025) 299-306.
24. Z. Sun, Chem. Eng. Trans. 66 (2018) 193-198.
25. Q. Tian, D. Sun, Z. Gu, and Z. Lv, J. Ceram. Process. Res. 21[3] (2020) 358-364.
26. J. Yu, F. Yu, X. Chen, S. Li, and H. Liu, Sci. Technol. Eng. 24[5] (2024) 2168-2176. (in Chinese)
27. S. Li, F. Yu, X. Chen, and H. Liu, Bull. Chin. Ceram. Soc. 42[11] (2023) 3964-4005.
28. S. Liu, F. Wang, G. Li, and Y. Wang, Acta Mater. Compos. Sin. 38[8] (2021) 2724-2736.
29. X. Cheng and J. Mu, J. Chin. Ceram. Soc. [4] (1962) 175-189. (in Chinese)
30. National Standardization Administration of China. GB/T 31289-2014: Portland cement used for ocean project [S]. Beijing: China Standards Press, 2014.
31. L. Wang, J.W. Song, Y. Ouyang, J.L. Zhu, and S.H. Liu, Concr. [4] (2018) 78-81.
32. F.Y. Li, Build. Mater. World 35[4] (2014) 6-9.
33. W.M. Tu, H.H. Peng, B.B. Xu, and Y.Z. Chen, J. Wuhan Univ. Technol. 29[6] (2007) 43-45.
34. D. Xia, C. Wu, K. Cui, and Y. Li, J. Southwest Jiaotong Univ. 59[5] (2024) 1113-1122. (in Chinese)
35. H. Sun, J. Qian, and S. Yang, J. Chin. Ceram. Soc. 45[5] (2017) 690-696.
36. T. Matschei, F. Bellmann, and J. Stark, Adv. Cem. Res. 17[4] (2005) 167-178.
37. Q. Zhao, M. Zhou, and H.B. Fischer, Cem. Guide New Epoch [6] (2008) 5-25. (in Chinese)
38. C. Cui, Y.B. Xie, and S.D. Zhu, Cem. [2] (2000) 13-16.
39. H. Ba, Z. Liu, and W. Chen, J. Chin. Ceram. Soc. [1] (2005) 36-41. (in Chinese)
40. State Administration for Market Regulation. (2021). Method of testing cements-determination of strength: GB/T 17671-2021. China Standard Press. (in Chinese)
41. State Administration for Market Regulation. (2019). Test method for seawater erosion resistance of cement: GB/T 38140-2019. China Standard Press. (in Chinese)
42. H. Liu, J. Zhou, W. Tian, and L. Zhang, J. Hebei Univ. Sci. Technol. 51[3] (2022) 80-86.
43. X. Han, in Experimental study on relationship between micro-porosity fractal characteristics and compressive strength of cement-based materials [Master's thesis], Shandong Agricultural University, 2019.
44. Z. Wu and H. Lian, Concr. [4] (2000) 4-7.
45. L. Wang, M. Jin, Y. Wu, Y. Zhou, and S. Tang, Constr. Build. Mater. 272 (2021) 121952.